

Article

Label-Free Assessment of Mannitol Accumulation Following Osmotic Blood–Brain Barrier Opening Using Chemical Exchange Saturation Transfer Magnetic Resonance Imaging

Jing Liu ^{1,2,3,†}, Chengyan Chu ^{4,†}, Jia Zhang ^{2,3}, Chongxue Bie ^{2,3}, Lin Chen ^{2,3}, Safiya Aafreen ⁵, Jiadi Xu ^{2,3}, David O. Kamson ^{6,7}, Peter C. M. van Zijl ^{2,3}, Piotr Walczak ⁴ , Mirosław Janowski ⁴  and Guanshu Liu ^{2,3,6,*} 

¹ Department of Radiology, The First Affiliated Hospital of Guangzhou Medical University, Guangzhou 510230, China

² Russell H. Morgan Department of Radiology and Radiological Sciences, Division of MR Research, The Johns Hopkins University School of Medicine, Baltimore, MD 21205, USA

³ F.M. Kirby Research Center for Functional Brain Imaging, Kennedy Krieger Institute, Baltimore, MD 21205, USA

⁴ Department of Diagnostic Radiology and Nuclear Medicine, University of Maryland, Baltimore, MD 21201, USA

⁵ Department of Biomedical Engineering, Johns Hopkins University, Baltimore, MD 21218, USA

⁶ The Sidney Kimmel Comprehensive Cancer Center, Johns Hopkins University, Baltimore, MD 21218, USA

⁷ Department of Neurology, Johns Hopkins University, Baltimore, MD 21218, USA

* Correspondence: guanshu@mri.jhu.edu; Tel.: +1-443-923-9500; Fax: +1-410-614-3147

† These authors contributed equally to this work.



Citation: Liu, J.; Chu, C.; Zhang, J.; Bie, C.; Chen, L.; Aafreen, S.; Xu, J.; Kamson, D.O.; van Zijl, P.C.M.; Walczak, P.; et al. Label-Free Assessment of Mannitol Accumulation Following Osmotic Blood–Brain Barrier Opening Using Chemical Exchange Saturation Transfer Magnetic Resonance Imaging. *Pharmaceutics* **2022**, *14*, 2529. <https://doi.org/10.3390/pharmaceutics14112529>

Academic Editor: Carlotta Marianecchi

Received: 17 October 2022

Accepted: 16 November 2022

Published: 20 November 2022

Publisher's Note: MDPI stays neutral with regard to jurisdictional claims in published maps and institutional affiliations.



Copyright: © 2022 by the authors. Licensee MDPI, Basel, Switzerland. This article is an open access article distributed under the terms and conditions of the Creative Commons Attribution (CC BY) license (<https://creativecommons.org/licenses/by/4.0/>).

Abstract: Purpose: Mannitol is a hyperosmolar agent for reducing intracranial pressure and inducing osmotic blood–brain barrier opening (OBBBO). There is a great clinical need for a non-invasive method to optimize the safety of mannitol dosing. The aim of this study was to develop a label-free Chemical Exchange Saturation Transfer (CEST)-based MRI approach for detecting intracranial accumulation of mannitol following OBBBO. Methods: In vitro MRI was conducted to measure the CEST properties of D-mannitol of different concentrations and pH. In vivo MRI and MRS measurements were conducted on Sprague–Dawley rats using a Biospec 11.7T horizontal MRI scanner. Rats were catheterized at the internal carotid artery (ICA) and randomly grouped to receive either 1 mL or 3 mL D-mannitol. CEST MR images were acquired before and at 20 min after the infusion. Results: In vitro MRI showed that mannitol has a strong, broad CEST contrast at around 0.8 ppm with a mM CEST MRI detectability. In vivo studies showed that CEST MRI could effectively detect mannitol in the brain. The low dose mannitol treatment led to OBBBO but no significant mannitol accumulation, whereas the high dose regimen resulted in both OBBBO and mannitol accumulation. The CEST MRI findings were consistent with ¹H-MRS and Gd-enhanced MRI assessments. Conclusion: We demonstrated that CEST MRI can be used for non-invasive, label-free detection of mannitol accumulation in the brain following BBBO treatment. This method may be useful as a rapid imaging tool to optimize the dosing of mannitol-based OBBBO and improve its safety and efficacy.

Keywords: CEST MRI; MRS; mannitol; BBBO treatment

1. Introduction

The blood–brain barrier (BBB) poses a major challenge in drug delivery into the central nervous system. For example, the fact that less than 2% of FDA approved anticancer drugs can pass the BBB is thought to be a major factor in the low success rate in brain cancer clinical trials [1,2]. Thus, there has been a recently renewed clinical interest in BBB opening methods to overcome these challenges. Mannitol is a sugar alcohol that has been used widely in the clinic as an intravenous (IV) hyperosmotic diuretic agent used for lowering intracranial and intraocular pressure (ICP) complicating traumatic brain

injury [3], stroke [4], brain tumors [5], and other conditions [6,7]. Intra-arterial (IA) infusion of mannitol results in local osmotic blood–brain barrier opening (OBBBO) in the cerebral vascular territory supplied by the catheter [8,9]. Since the first Phase I clinical trial in 1979 [10], many clinical studies have shown that, combined with OBBBO, intra-arterial (IA) drug infusion can effectively improve CNS delivery of chemotherapy drugs [11]. For example, Charest et al., showed that combined IA-drug infusion and mannitol-based OBBBO generated an overall 2-fold higher carboplatin concentrations in brain tumors compared to IA infusion alone [12]. Thus, for agents that cannot cross the BBB naturally, such as antibodies or nanobodies, there is a great clinical demand for the development of quantitative imaging biomarkers that could provide spatial information about the extent of BBB opening and drug delivery [13,14].

While numerous new strategies to deliver drugs beyond the BBB have been explored to date, such as microbubble-based high-intensity focused ultrasound (HIFU) and convection-enhanced delivery (CED), or receptor-mediated transcytosis (RMT), mannitol-based OBBBO is still considered an effective and safe approach that is continuously used in the clinic [15]. However, the current mainstay of X-ray guidance of OBBBO procedures lacks spatial selectivity and may not detect off-target OBBBO and possible unwanted adverse effects in normal brain parenchyma. To overcome this limitation, contrast-based MRI methods are being developed to pre-determine the regions affected by IA-injected mannitol and to provide image-guidance for fine-tuning key injection parameters to achieve precisely controlled OBBBO in desired areas [16–19]. Real-time MRI has been also used to navigate OBBBO in a patient with brain cancer [20,21].

A critical hindrance to the widespread use of IA-injection of mannitol in the brain is the potential of mannitol deposition following OBBBO. It is well known that the accumulation of mannitol in the brain interstitium can cause a “rebound” phenomenon, i.e., a secondary reversal of the osmotic gradient and an increase in brain water content, followed by increased ICP [22,23]. This can be caused by either prolonged or repeated dosing [24,25]. However, in infiltrative brain tumors, interstitial mannitol concentrations many folds higher than in the plasma can be observed even after a single intravenous bolus injection [26]. Thus, the dose and frequency of mannitol administration need to be carefully planned and monitored to avoid this potential side effect while maintaining treatment efficacy. Clinically, either serum osmolarity or osmolar gap are used as surrogate measures of serum mannitol concentration [7]. The osmolality is directly measured by the concentration of solutes per kilogram of solvent (mOsm/kg), and the osmotic (osmole, or osmolal) gap is calculated by the difference between osmolality and osmolarity, the calculated value of the concentration of solutes per liter of solvent (mOsm/L). An osmolality of 320 mOsm/kg and an osmolar gap of 20–55 mOsm/kg were suggested to be the highest safe serum mannitol level [27]. However, neither of these surrogate measures reflect absolute values of serum mannitol, making it difficult for clinicians to closely monitor intravascular volume status and renal function during mannitol therapy. A few previous studies reported the use of ^1H magnetic resonance spectroscopy (MRS) and magnetic resonance spectroscopic imaging (MRSI) for detecting mannitol [28–30]. However, a low spatial resolution and a relatively long acquisition time hamper the clinical application of MRS/MRSI. Therefore, a new non-invasive method that can reliably and rapidly assess the amount and spatial distribution of mannitol accumulation in the brain is needed.

This study aimed to develop an MRI approach for detecting mannitol accumulated in the brain following OBBBO. The mannitol molecule contains six hydroxyl(-OH) protons, which can be directly detected by Chemical Exchange Saturation Transfer (CEST) without the need for chemical labeling [31]. CEST MRI is an emerging technology wherein the MRI contrast is generated by transferring the selectively saturated MR signal of exchangeable protons to their surrounding water protons through the process of chemical exchange [32]. Mounting studies have shown the ability of CEST MRI to detect hydroxyl-protons containing molecules such as glucose [33–35], 2-deoxy-D-glucose (2-DG) [36–38], 3-O-methyl-D-glucose (3OMG) [39,40], glucosamine [41], dextrans [42–45], and many others [46,47]. Some of these

methods have entered patient studies [48,49]. Herein, we investigated the ability of CEST MRI to detect the tissue accumulation of mannitol at a high spatial resolution, which will provide a valuable imaging tool for optimizing mannitol-based BBBO treatments by controlling the dose of mannitol to prevent unintended mannitol leakage to the brain parenchyma.

2. Materials and Methods

2.1. Chemicals

Unless otherwise noted, all chemicals were purchased from Sigma Aldrich (St. Louis, MO, USA). The D-mannitol (25% solution) used in animal studies was purchased from Hospira Inc. (Hospira Inc., Lake Forest, IL, USA).

2.2. Animals

All animal protocols were approved by our Institutional Animal Care and Use Committee. Sprague-Dawley rats (male, 200–250 g) were purchased from Charles River (Watershed, MA, USA). Catheterization was performed as previously described [16,50]. In brief, rats were anesthetized under 2% isoflurane and fixed in the supine position, followed by dissection of the common carotid artery (CCA) bifurcation. The external carotid artery (ECA) and pterygopalatine artery (PPA) were temporarily ligated with 4–0 silk sutures to permit all the solutions to enter the cerebrum. A small arteriotomy in the CCA was made, and a catheter (VAH-PU-C20, Instech Solomon Inc., Plymouth Meeting, PA USA) connected to #30 PTFE tubing was introduced into the internal carotid artery (ICA). The intra-arterial catheter was secured with the animal during MRI scans. Rats were randomly separated into two groups ($n = 3$ each) to receive either 1 mL or 3 mL D-mannitol at a 0.6 mL/min rate. The corresponding infusion time and total doses were 1.7 min (4 mL/kg or 1 g/kg) and 5 min (12 mL/kg or 3 g/kg), respectively.

2.3. $^1\text{H-NMR}$

The $^1\text{H-NMR}$ measurements of mannitol solutions (100 mM in D_2O or a mixture of 90% H_2O and 10% D_2O) were performed on a Bruker Avance III 500 MHz spectrometer (Bruker Biosciences, Billerica, MA, USA) at room temperature (pH = 6.5). The ^1H NMR spectra were acquired using a standard one-dimensional pulse sequence (zg30) with 128 scans. A total of 65,500 data points for each scan were acquired with a spectral width of 20.6 ppm and an acquisition time of 3.18 s. The data were recorded and processed with TopSpin 4.0.1.

2.4. *In Vitro* MRI

In vitro MRI was conducted to measure the CEST properties and T_1 and T_2 relaxation times of D-mannitol in PBS solution of different concentrations (5 to 100 mM) and pH (5.5 to 8.0) using a 11.7T Bruker Avance vertical bore MRI system equipped with a 15 mm saw-tooth RF coil (Bruker Biosciences, Billerica, MA, USA). CEST MRI was conducted using a modified rapid acquisition with relaxation enhancement (RARE) sequence as described previously [44,51]. Z-spectral data were acquired by varying the offset of saturation pulses from -4 ppm to 4 ppm with respect to the water resonance (0 ppm) using an increment of 0.2 ppm, with the S_0 image was acquired using $B_1 = 0$ μT at -50 ppm. Unless otherwise noted, the parameters of the saturation RF pulses were continuous wave (CW), $T_{\text{sat}} = 3000$ ms, $B_1 = 1.8$ μT (150 Hz). Other imaging parameters were: TR/TE = 6.0 s/5 ms, RARE factor = 16, slice thickness = 2 mm, matrix size = 64×64 , FOV = 15×15 mm², spatial resolution = 0.23×0.23 mm², number of averages (NA) = 2, total acquisition time = 16 min 48 s. The B_0 inhomogeneity was measured using the Water Saturation Shift Reference (WASSR) method [52] using the same parameters as those used in CEST imaging except TR = 1.5 s, $T_{\text{sat}} = 500$ ms, $B_1 = 0.5$ μT (21.3 Hz) and the saturation frequency swept from -1 ppm to 1 ppm (step size = 0.1 ppm). T_1 and T_2 maps were acquired as described previously [16,53] using a RARE-based saturation recovery sequence with eight TR values ranging between 200 ms and 15,000 ms (TE = 4.3 ms and RARE factor = 4, central encoding), and a modified RARE pulse sequence (TR/TE = 25,000/4.3 ms and RARE factor = 16) with a Carr-Purcell-Meiboom-Gill (CPMG) T_2 preparation module

($t_{\text{CPMG}} = 10$ ms, the number of CPMG loops ranging from 2 to 1024, corresponding to echo times = 20 ms to 10.24 s), respectively. During MRI scans, the temperature of the samples was maintained at 37 °C.

2.5. In Vivo MRI

All in vivo studies were conducted on a Biospec 11.7T horizontal MRI scanner (Bruker Biosciences, Billerica, MA, USA) equipped with a rat brain surface array RF coil (receiver) and a 72 mm volume coil (T11232V3, transmitter). All CEST MR images were acquired using the same RARE-CEST sequence (CW saturation pulse: $B_1 = 1.8$ μT , $T_{\text{sat}} = 3$ s, TR/TE = 5000/5 ms, RARE factor = 23, matrix size = 64×64 (with partial FT acceleration to 64×23), FOV = 30×30 mm², spatial resolution = 0.47×0.47 mm², slice thickness = 0.6 mm, number of averages NA = 2, acquisition time = 8 m 40 s). Z-spectral acquisitions were acquired by sweeping saturation offsets (CW pulse, $B_1 = 1.8$ μT , $T_{\text{sat}} = 3$ s) from -5 to $+5$ ppm (step=0.2 ppm) before and at 20 min after the infusion of mannitol at the prescribed volumes. The time interval of 20 min was chosen because the half-life of mannitol in rats was estimated to be 17–25 min using the reported human values of 70–100 min [54,55] and a scaling method reported by Obach and colleagues [56]. The WASSR method was also acquired to correct B_0 inhomogeneity.

T_1 and T_2 maps were acquired using the same geometry as the CEST MRI. In brief, T_1 maps were assessed using a RARE-based saturation recovery sequence with six TR values ranging between 375 ms and 7,500 ms; TE = 11.3 ms and RARE factor = 4, central encoding, acquisition time = 3 m 47 s. T_2 maps were acquired using a multi-slice/multi-echo (MSME) sequence (TR = 2200, 30 TE values ranging from 7.5 to 225 ms, acquisition time = 2 m 21 s).

Following the post-mannitol CEST acquisition, single-voxel localized ¹H MRS spectra (voxel size = $4 \times 6 \times 3$ mm³) were acquired in the ipsilateral and contralateral hemispheres using a stimulated echo acquisition mode (STEAM) sequence (TE = 4 ms, TM = 10 ms, TR = 2.5 s, NA = 64, acquisition time = 2 m 40 s) with outer volume suppression (OVS) and the variable power RF pulses and optimized relaxation delays (VAPOR) water suppression scheme according to previously published procedure [57]. A field mapping method was used to adjust the first-and second-order shims before MRS acquisition.

2.6. Data Processing

All MRI data processing was performed using custom-written scripts in MATLAB (Mathworks, Waltham, MA, USA). For CEST MRI data, pixel-wise B_0 correction was conducted first. Then a region of interest (ROI) mask was placed over each sample, and the mean value of water signal intensity ($S^{\Delta\omega}$) at each saturation offset relative to the water protons ($\pm\Delta\omega$) was calculated. The normalized $S^{\Delta\omega}/S_0$, where S_0 is the water signal intensity without saturation, was plotted as a function of $\Delta\omega$, which is traditionally called a Z-spectrum. To quantify the CEST effect, the magnetization transfer ratio asymmetry (MTR_{asym}) was calculated as $\text{MTR}_{\text{asym}} = (S^{-\Delta\omega} - S^{+\Delta\omega})/S_0$. As the peak position of MTR_{asym} plots is dependent of the concentration of mannitol due to interference of the direct saturation, we used numerically integrated area under the curve (AUC) [58] of MTR_{asym} plots between 0.2 and 2 ppm as an approximation of the signal integral. Because AUC values are also dependent on the frequency range, we normalized the AUC values by the spectral width (ppm) that used in the calculation. The resulting AUC values have a unit of % per ppm (%/ppm).

To accurately quantify the CEST effect in the presence of substantial T_1 changes, the T_1 compensated inverse Z-analysis (AREX), defined by $(S_0/S^{+\Delta\omega} - S_0/S^{-\Delta\omega})/T_1$, were also calculated using the acquired T_1 times [59–61]. Of note, because the AREX values were calculated to quantify the asymmetry between the water signals at two offsets with respect to water resonance, it actually should be called AREX_{asym}.

To quantify the concentration of mannitol in different tissues, we also fitted the Z-spectra using 6-pool Bloch equations as described previously [62–64]. To reduce the computing time and increase the reliability of fitting, we performed Bloch fitting in two steps. First, we fitted using the ROI values of ipsilateral and contralateral hemispheres,

which had higher SNR compared to those of individual pixels. In the fitting, water R_{1A} (experimentally measured), the offsets of amide, amine, and magnetization transfer contrast (MTC) pools, and the T_2 times of all the exchangeable protons (except the NOE pool) were fixed, with all other parameters set to fitting parameters. Table 1 lists the starting or fixed values according to those reported in the literature [65]. Then, the fitted exchange rates of all pools, T_2 relaxation time of the NOE pool, and concentrations of amide and NOE from the first step ROI fitting were fixed in the second step pixel-by-pixel fitting.

Table 1. List of the starting or fixed values of the parameters used in Bloch fitting.

	Hydroxyl	Amine/Guanidinium	Amide	NOE	MTC
Proton concentration (mM)	45	100	72	100	5500
Exchange rate (Hz)	1400	1100	30	16	15
Offset (ppm)	0.9	2	3.5	−3.5	−2.3
T_2 (ms)	55	170	100	5	9.1×10^{-3}
T_1 (s)	1	1	1	1	1

Italic/bold numbers indicate those values were fixed in the fitting.

In vivo ^1H -MRS was processed according to a previously published procedure [66]. As a reference for chemical shifts, the *N*-acetyl-aspartate (NAA) resonance was set at 2.02 ppm. After local baseline flattening around the integration region using a second-order polynomial baseline correction, the peaks at 3.03 ppm and 3.5–4 ppm (total creatine (tCr) and mannitol, respectively), were quantified using their integrated peak areas.

2.7. Statistical Analysis

Data were expressed as mean \pm SD. The comparison of two groups was conducted using a two-tailed Student's *t*-test.

3. Results

3.1. CEST Characteristics of mannitol

We first acquired and compared the NMR spectra of D-mannitol (100 mM, pH 6.5, room temperature) in $\text{H}_2\text{O}/\text{D}_2\text{O}$ and D_2O . Mannitol contains six exchangeable protons (red in Figure 1a) and eight non-exchangeable protons (blue in Figure 1a). As shown in Figure 1b, both exchangeable and non-exchangeable protons appeared in the H_2O NMR spectrum, whereas only non-exchangeable protons were distinguishable in the D_2O NMR spectrum. A broad signal of hydroxyl protons could be observed between 5.1 and 5.7 ppm, corresponding to offsets of 0.4 to 1.0 ppm with respect to the resonance of water (4.7 ppm). Four distinct NMR signals of non-exchangeable protons with distinct scalar coupling patterns were observed in both D_2O and H_2O NMR spectra, at approximately 3.65, 3.73, 3.77, and 3.84 ppm, in good agreement with previous reports [67]. Figure 1c shows a merged peak of water and OH signal in the Z-spectrum of 20 mM mannitol and a broad MTR_{asym} peak between 0.2 and 2 ppm. It is be (in the intermediate to fast exchange regime), leading to a distinct signal broadening especially at positive frequency and.

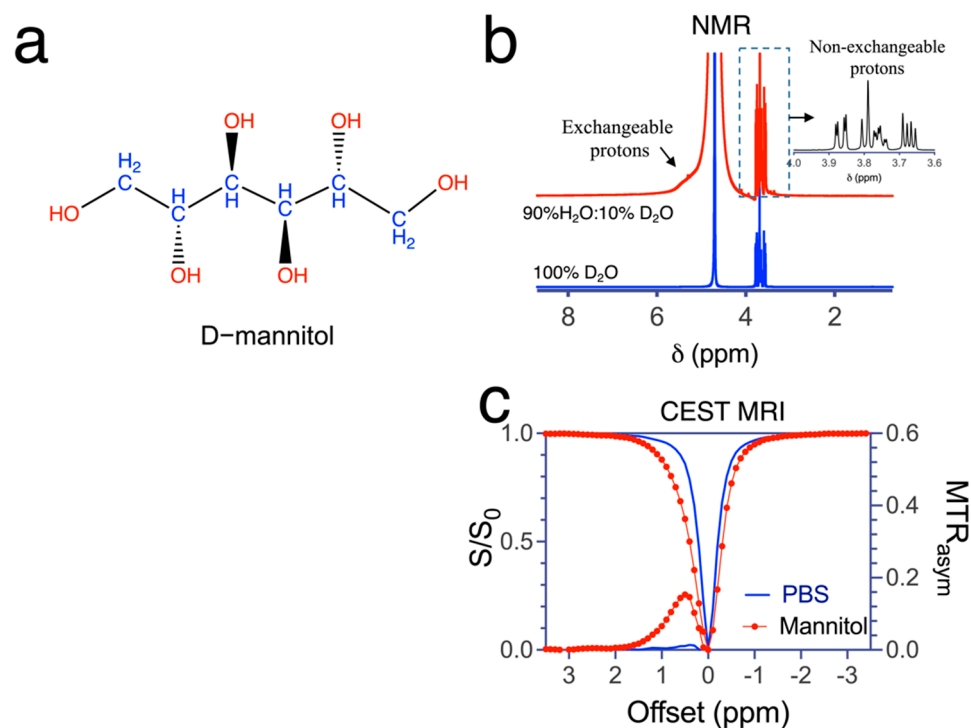


Figure 1. NMR and CEST MRI signal of mannitol (a) Chemical structure of mannitol. Red: functional groups containing exchangeable protons; blue: functional groups containing non-exchangeable protons. (b) NMR spectra of 100 mM mannitol (pH 6.5) in D₂O (bottom, blue line) and H₂O (top, red line, H₂O: D₂O = 90%:10%) at pH = 7.4 and room temperature. (c) Z-spectra and MTR_{asymp} plots of 20 mM mannitol (PBS solution, pH 7.2, 37 °C) in PBS and blank PBS solution. CEST MRI was acquired using a CW pulse ($B_1 = 1.8 \mu\text{T}$ and $T_{\text{sat}} = 4 \text{ s}$).

Subsequently, we characterized the CEST contrast of mannitol as a function of concentration and pH. As shown in Figure 2a, the CEST contrast of mannitol increases with concentration. The apparent peak position of the MTR_{asymp} curve is around 0.4 ppm at 1 mM and shifts to higher offsets at higher concentrations, i.e., 0.6 ppm at 40 mM. Quantified by the AUC (0.2–2 ppm) of the MTR_{asymp} plots, the mannitol CEST contrast is linearly correlated with concentration (Figure 2b, $R^2 = 0.9927$). Fitting the Z-spectra to the Bloch equations allows more accurate estimation of the mannitol concentration for the faster exchange rates (Figure 2c, $R^2 = 0.9976$). Based on the curves in Figure 2b,c, the detectability of CEST MRI for mannitol is estimated to be approximately 1 mM to generate $0.25 \pm 0.01\%$ per ppm CEST contrast (AUC (0.2–2 ppm)). Similar to D-glucose [34,35], the mannitol has CEST contrast that is sensitive to pH (Figure 2d,e) and decreases markedly with increasing pH for pH values above 6.5, attributed to the increased exchange rates and the faster exchange regime at higher pH. The CEST contrast at pH 6.5 was approximately 1.6 times higher than that at pH 7.2, with AUC values of 10.4 ± 0.2 and $16.7 \pm 0.1\%$ per ppm, respectively. The CEST contrasts at pH 5.5 and 6.0 (AUC = $5.8 \pm 0.1\%$ and $8.8 \pm 0.2\%$ per ppm, respectively) were smaller than that of pH 6.5, likely due to the shift from base-catalyzed to acid-catalyzed exchange regime. Using Bloch equation fitting of Z-spectra acquired at various B_1 values (Figure S1), we estimated the exchange rates (k_{ex}) of mannitol as a function of pH (Figure 2f), which showed that the exchange rate increases gradually between pH 6.5 and 8.0. Even at pH 6.5, the k_{ex} was estimated to be 1167 s^{-1} , which would still be considered intermediate, given the offset of 0.8 ppm ($\Delta\omega = 0.8 \text{ ppm} \times 500 \text{ (s}^{-1}/\text{ppm)} \times 2\pi \text{ (rad)} \approx 2500 \text{ rad/s}$).

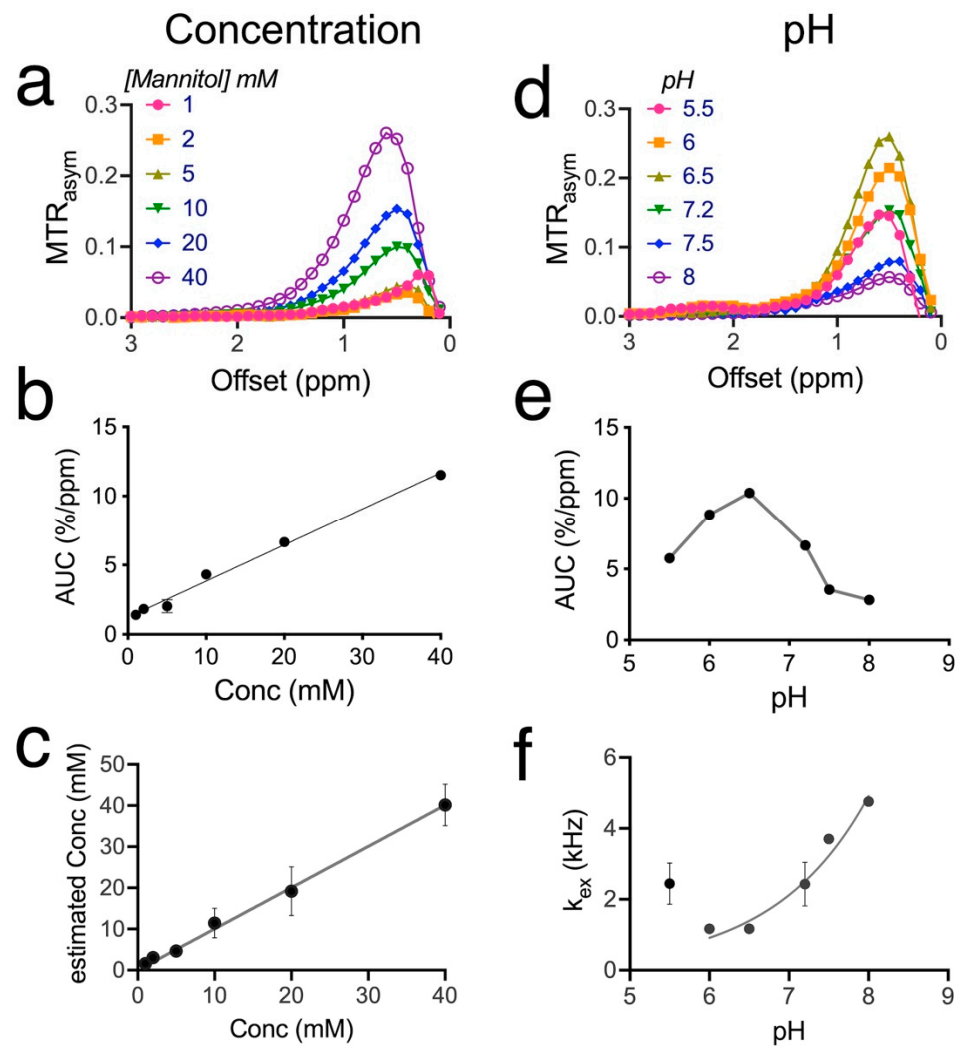


Figure 2. Concentration and pH dependence of the CEST MRI contrast of mannitol at 11.7T (37 °C). (a) MTR_{asym} plots of mannitol at concentrations ranging from 1 to 40 mM (pH 7.2 in PBS). (b) Concentration dependence of mannitol CEST contrast as quantified by AUC (0.2–2 ppm). (c) Linear correlation between the concentrations estimated using Bloch equation fitting and the nominal concentrations. (d) MTR_{asym} plots of mannitol solutions as a function of pH (20 mM in PBS). (e) pH dependence of mannitol CEST contrast as quantified by AUC (0.2–2 ppm). (f) Exchange rates of hydroxyl protons as a function of pH. Unless otherwise noted, all CEST experiments were acquired using a RARE sequence (TR/TE = 6000/5 ms) and a CW saturation pulse ($B_1/T_{sat} = 1.8 \mu T/4$ s).

The absolute CEST contrast is also impacted by the choice of acquisition parameters, including T_{sat} and B_1 , which were also studied (Figure S2). It should be noted that, while $3.6 \mu T$ appeared to be the optimal B_1 for in vitro detection, we used a lower B_1 value later in in vivo studies to reduce the MTC effect that may interfere with in vivo quantification. Finally, we also measured the r_1 and r_2 relaxivities of mannitol, which were $2.3 \times 10^{-5} s^{-1} mM^{-1}$ and $5.7 \times 10^{-2} s^{-1} mM^{-1}$ (pH = 7.2 and 37 °C), respectively (Figure S3), suggesting that mannitol causes a negligible T_1 concentration effect and a noticeable T_2 effect, similar to D-glucose [68].

3.2. Mannitol Excess Causes Extravasation and Brain Accumulation of Mannitol

We first investigated whether IA infusion of an excess amount of mannitol (at the ICA as illustrated in Figure 3a) could cause accumulation of mannitol in the injected hemisphere. We intermittently injected different volumes of 1374 mM (25% mannitol solution) intra-arterially and used 1H -MRS to detect brain uptake reflected in strongly increased aliphatic 1H signals

in the range of 3.6–3.9 ppm (Figure 3b). Total mannitol concentration was estimated from the ratio of the integral of these aliphatic protons of mannitol (3.6–3.9 ppm, eight protons) with those of the integral total creatine at 3.03 ppm (assumed to be 9 mM [69], three protons). The mannitol concentrations in the brain were then calculated using a 0.34/11.7 mL blood to the total brain volume in the brain of rats [70] and a blood concentration of mannitol that was calculated using the injection volume (0.5 to 5 mL) and an average whole-body blood volume of 20.7 mL [70]. The quantitative MRS measures are shown in Figure 3c, which indicate a two-phase increase in the concentration of mannitol in the brain: an initially slow and linear increase phase in the injection volume range up to 2 mL, followed by a dramatic exponential increase phase when injection volume exceeded 2 mL. The leaked mannitol concentration reached a high level (>70 mM) when 5 mL mannitol was infused.

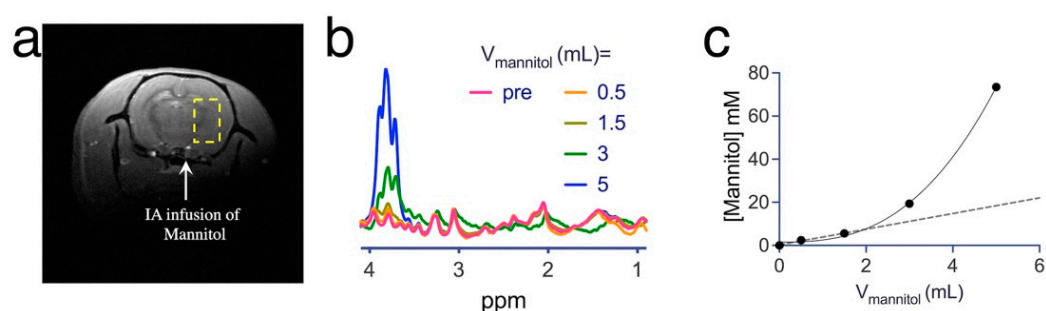


Figure 3. MRS assessment of the brain accumulation of administered mannitol (25% *w/w*). (a) Representative T_{2w} anatomical image showing the location of intra-arterial (IA) infusion (white arrow) of mannitol and the voxel (yellow dashed line) for ^1H -MRS measurement. (b) ^1H -MRS spectra as a function of the injection volume of mannitol. (c) Calculated mannitol concentration (mM) in the brain as a function of injection volume, where dash line is the linear regression of the first three data points of low doses.

3.3. MRI Manifestations following Mannitol Accumulation in the Brain

We subsequently conducted a comprehensive MR assessment, including CEST, T_1 , and T_2 mapping, and ^1H -MRS (Figure 4a), of rats receiving mannitol treatment at either low or high dose, i.e., injection volumes = 1 and 3 mL, respectively. The blood concentrations of mannitol were calculated to be 63 and 174 mM, respectively. At the end of each study, Gd-based contrast-enhanced MRI was also conducted to assess the area of BBB breakdown. Figure 4b shows the parametric maps of MRI contrast changes in representative rats from the two groups. It can be seen that IA infusion of mannitol at a low dose (1 mL) did not cause noticeable changes in CEST and T_1 contrast. However, slightly increased R_2 was observed in some of the regions.

Conversely, injecting an excessive amount of mannitol (3 mL) resulted in marked changes in CEST contrast, indicating the accumulation of mannitol at the injection site, which was confirmed by ^1H -MRS observation. There were also markedly decreased R_1 and R_2 relaxation rates in the ipsilateral hemisphere, attributable to severe edema caused by the tissue accumulation of mannitol. Finally, the regions undergoing BBBO were rendered by Gd-based contrast-enhanced MRI, which revealed that, while both doses resulted in BBBO, the higher dose produced a much larger area of BBBO. In the high dose group, the BBBO regions appeared to be similar to those areas with increased mannitol-CEST contrast or those of decreased ΔR_1 , but larger than those of decreased ΔR_2 . In both groups, mannitol did not cause noticeable MRI contrast changes in the contralateral side, indicative of a negligible impact of mannitol infusion on the “off-target” regions.

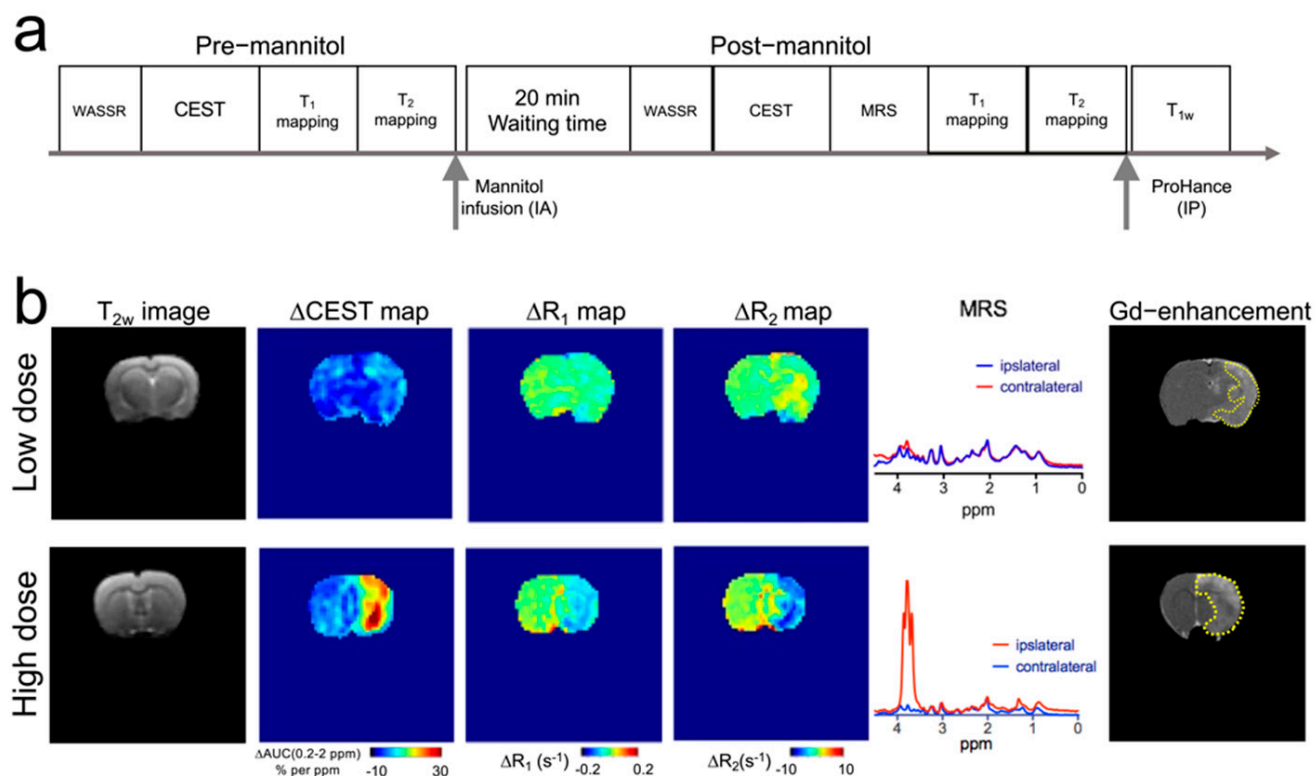


Figure 4. CEST, R_1 , R_2 , Gd-enhanced and MRS contrast changes caused by mannitol injected at low (1 mL) and high (3 mL) of 25% mannitol solution. (a) Schematic of the timeline of MRI acquisitions. (b) Representative images of the same slice showing (from left to right) T_2 -weighted anatomical images, CEST contrast parametric maps as quantified by ΔAUC (0.2–2 ppm), ΔR_1 contrast parametric maps, ΔR_2 contrast parametric maps; 1H MRS spectra, and Gd-based contrast-enhanced images of rats receiving low and high dose mannitol injection.

3.4. CEST MRI Detection of Mannitol in the Brain

We performed a quantitative analysis of the change in CEST contrast in different brain regions at about 20 min after mannitol infusion. As shown in Figure 5a, in rats that received high dose (3 mL) mannitol, there was a dramatic change in the mean Z-spectra of the ipsilateral hemisphere. No contrast change could be observed in the contralateral hemisphere. A main change in post-mannitol Z-spectra in the ipsilateral hemisphere was greatly reduced saturation transfer effect throughout the spectrum. On the contrary, MTR_{asym} analysis (Figure 5b) revealed a remarkable increase in CEST signal over the broad offset range corresponding to the mannitol hydroxyl signals. The AUC (0.2–2 ppm) parametric maps (Figure 5c) showed that the spatial distribution of increased CEST signal. The pre- and post-mannitol AUC (0.2–2 ppm) values (for the rat shown in Figure 5) were $20.1 \pm 4.1\%/ppm$ and $28.6 \pm 5.1\%/ppm$ in the ipsilateral hemisphere ($p = 0.0433$) and $20.0 \pm 2.4\%/ppm$ and $18.7 \pm 2.6\%/ppm$ in the contralateral hemisphere ($p = 0.3787$), respectively. In contrast, no significant change in CEST contrast was observed in the rats infused with 1 mL of 25% mannitol solution (Figure 6).

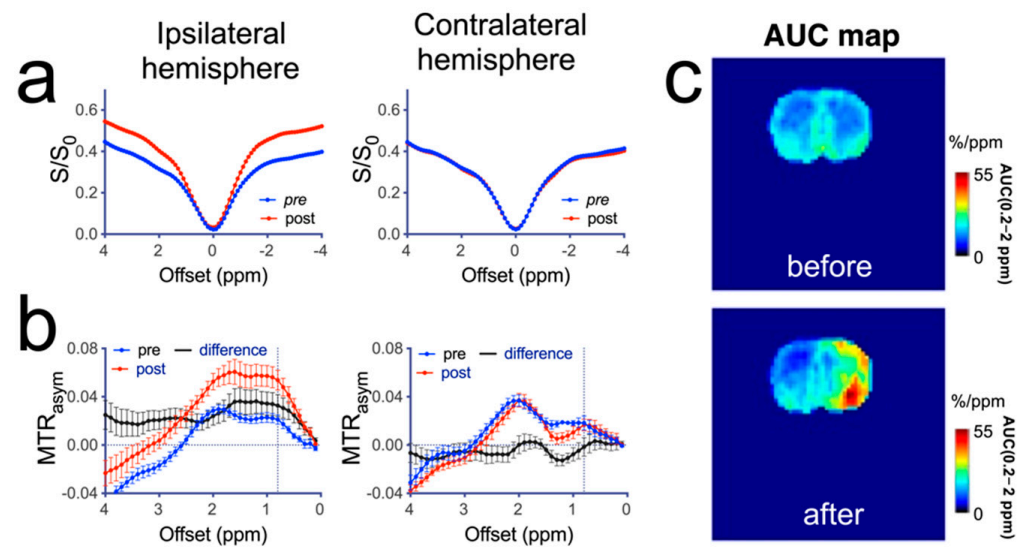


Figure 5. Quantitative analysis of CEST contrast in a representative rat infused with high dose (3 mL) of 25% mannitol solution. (a) Z-spectra obtained pre- and post-mannitol infusion in the ipsilateral (right) and contralateral (left) hemispheres. (b) MTR_{asym} plots of pre- and post-mannitol infusion in the ipsilateral (right) and contralateral (left) hemispheres. (c) AUC (0.2–2.0 ppm) maps before and after the infusion of mannitol.

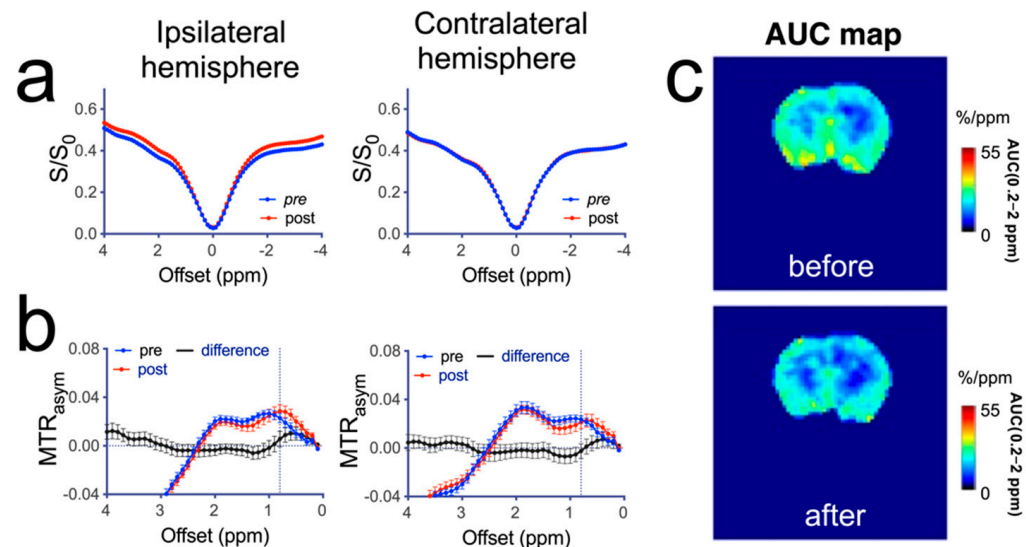


Figure 6. Quantitative analysis of CEST contrast in a representative rat infused with low dose (1 mL) of 25% mannitol solution. (a) Z-spectra of pre- and post-mannitol infusion in the ipsilateral (right) and contralateral (left) hemispheres. (b) MTR_{asym} plots of pre- and post-mannitol infusion in the ipsilateral (right) and contralateral (left) hemispheres. (c) AUC (0.2–2.0 ppm) maps before and after the infusion of mannitol.

Figure 7 compares the mean CEST contrast changes in the two cohorts ($n = 3$ in each group). The histogram analysis shows that the CEST signals of the voxels in the high dose group were substantially increased, indicating mannitol accumulation. In addition, the mean ΔAUC (0.2–2.0 ppm) values were significantly higher in the ipsilateral hemisphere than contralaterally in rats that received 3 mL 25% mannitol (Figure 7b, 12.54 ± 4.23 vs. 1.34 ± 6.12 %/ppm, $p = 0.0105$), while there was no significant difference in the low dose group (Figure 7d, -3.88 ± 3.40 vs. -1.63 ± 3.95 %/ppm, $p = 0.3536$).

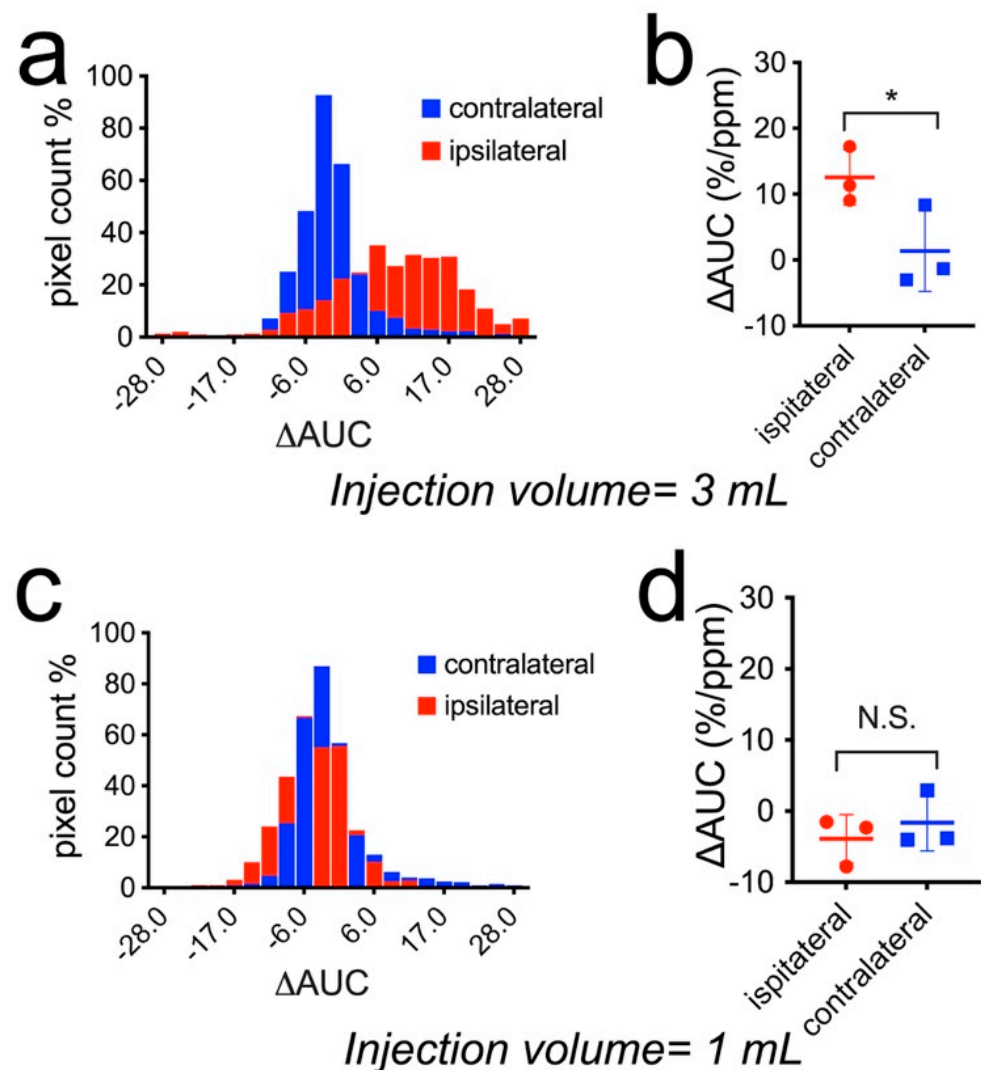


Figure 7. Comparison of the change in CEST contrast (ΔAUC (0.2–2.0 ppm)) in the ipsilateral and contralateral hemispheres after the injection of different doses of mannitol. (a) Histogram and (b) Mean values of three rats injected with 3 mL 25% mannitol. *: $p < 0.05$ ($p = 0.0105$, paired two-tailed Student t -test, $n = 3$). (c) Histogram and (d) Mean values of three rats injected with 1 mL 25% mannitol. N.S.: not significant ($p = 0.3536$, paired two-tailed Student t -test, $n = 3$).

To accurately quantify the CEST effect in the presence of substantial T_1 changes, we also attempted to quantify the CEST contrast enhancement by mannitol using the AREX approach. Figure 8a,b show the AREX (or AREX_{asym}) plots in the ipsilateral and contralateral hemispheres in a rat receiving high dose mannitol. Comparing the ΔMTR_{asym} (0.8 ppm) maps (Figure 8c) and $\Delta AREX$ (0.8 ppm) map (Figure 8d) reveals good agreement between the spatial distribution of $\Delta CEST$ signal by the two methods although the CEST contrast enhancement calculated by the MTR_{asym} method (i.e., 0.021 ± 0.003 vs. 0.054 ± 0.008 for pre- and post-mannitol, respectively, corresponding to an increase of 157% in CEST contrast) was higher than that by the AREX method (i.e., 0.318 ± 0.07 vs. 0.477 ± 0.05 for pre- and post-mannitol, respectively, corresponding to an increase of 50% in CEST contrast), attributed to T_1 “contamination” in the MTR_{asym} method.

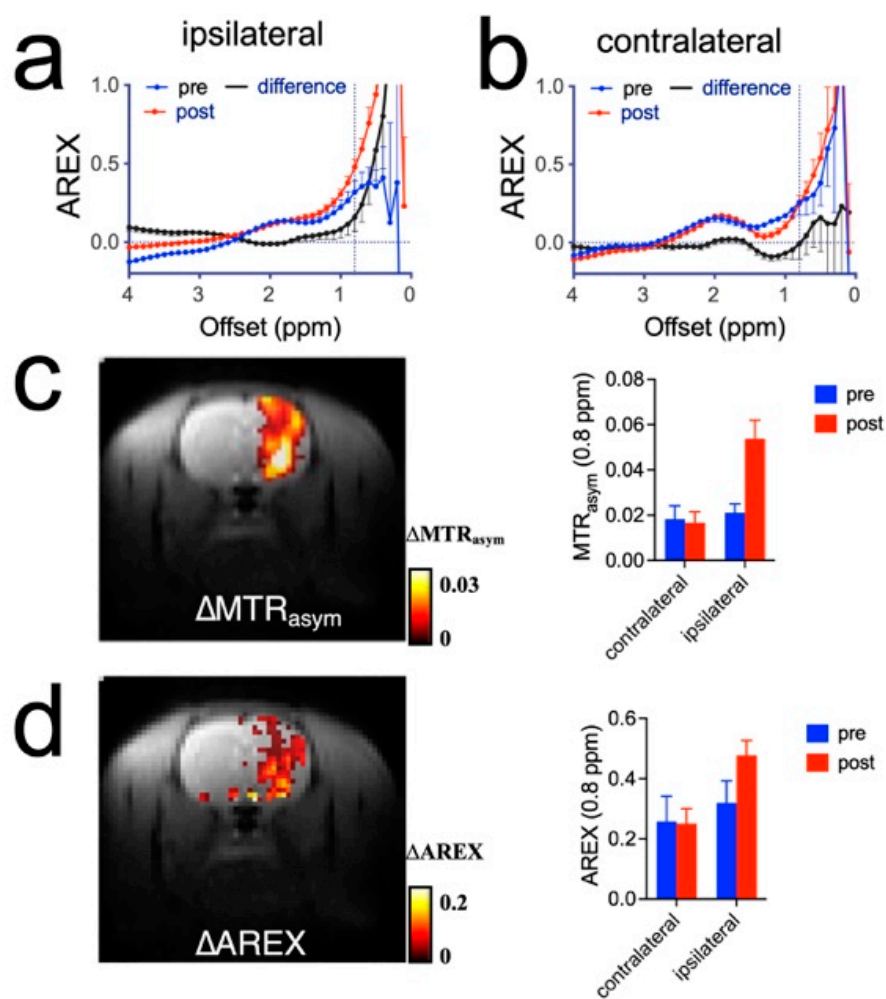


Figure 8. AREX analysis of rats infused with high dose (3 mL 25%) mannitol solution. (a) AREX plots of pre- and post-mannitol infusion in the ipsilateral hemisphere in a representative rat. (b) AREX plots of pre- and post-mannitol infusion in the contralateral hemisphere of the same rat. (c) Overlay image of T_{2w} image and ΔMTR_{asym} (0.8 ppm) parametric map (left) and the corresponding mean MTR_{asym} (0.8 ppm) in each hemisphere (right). (d) Overlay image of T_{2w} image and $\Delta AREX$ (0.8 ppm) parametric map (left) and the corresponding mean MTR_{asym} (0.8 ppm) in each hemisphere (right).

The comparison of the mean $\Delta AREX$ values between the low and high dose groups ($n = 3$ each) is shown in Figure 9. The histogram analysis shows that the CEST signals of the voxels in the high dose group were substantially inclined, indicating mannitol accumulation. In addition, the mean $\Delta AREX$ values were significantly higher in the ipsilateral hemispheres than those in the contralateral hemisphere in rats that received 3 mL 25% mannitol (Figure 9b, 0.147 ± 0.036 vs. -0.023 ± 0.015 , $p = 0.0237$), while there was no significant difference in the low dose group (Figure 9d, -0.049 ± 0.032 vs. -0.037 ± 0.049 , $p = 0.4297$).

Finally, we also attempted to quantify the CEST effect using Bloch fitting of the acquired CEST Z-spectral data together with T_1 and T_2 data (Figure S4) to compute the average concentration of mannitol in the two hemispheres. The average ipsilateral mannitol concentration in the high dose group ($n = 3$) was estimated to be 23.8 ± 17.8 mM, which is in good agreement with that measured by the MRS method (24.1 ± 4.9 mM), whereas the average concentration of mannitol was estimated to be 4.5 ± 3.7 mM in the low dose group ($n = 3$).

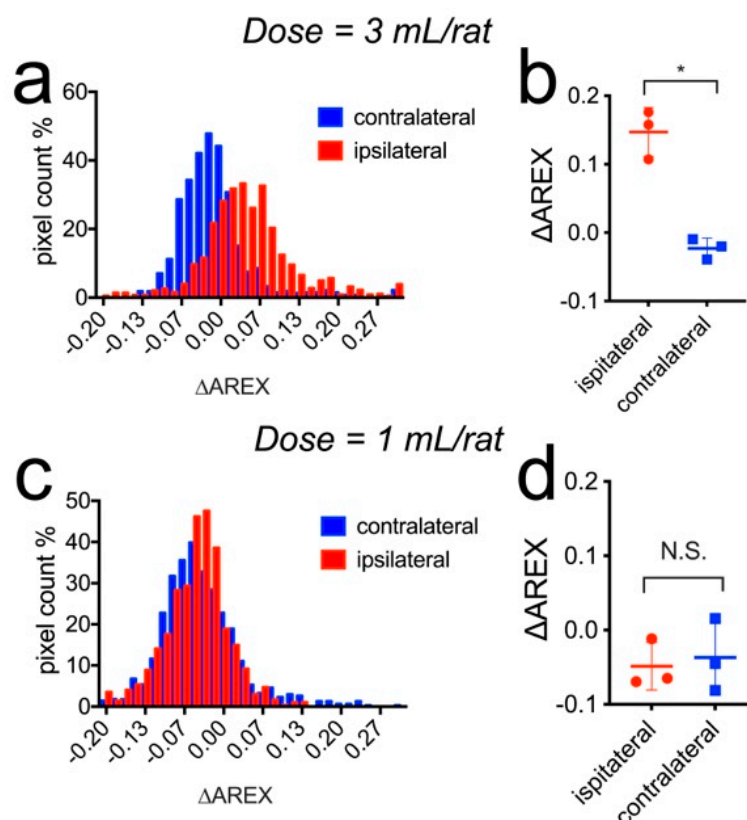


Figure 9. Comparison of the change in CEST contrast (Δ AREX) in the ipsilateral and contralateral hemispheres after the injection of mannitol at different doses. (a) Histogram and (b) Mean values of three rats injected with 3 mL 25% mannitol. *: $p = 0.0237$, paired two-tailed Student t -test, $n = 3$. (c) Histogram and (d) Mean values of three rats injected with 1 mL 25% mannitol. N.S.: $p = 0.4297$, paired two-tailed Student t -test, $n = 3$.

4. Discussion

In the present study, we systematically characterized the inherent CEST MRI contrast of mannitol *in vitro* and exploited it for non-invasive and label-free detection of mannitol accumulated in the brain following intra-arterial infusion for OBBBO. While mannitol has been used as a hyperosmotic agent for various medical applications, including OBBBO, it can cause severe adverse events in some patients (especially those with renal dysfunction), including electrolyte abnormalities, acidosis, hypotension, acute renal failure congestive, and heart failure with pulmonary edema [71–74]. Mannitol has been widely used to reduce ICP in the context of progressive symptomatic brain edema. Mounting evidence shows the correlation between excessive use of mannitol and mannitol accumulation in the areas of trauma, infarction, and tumors, where the BBB is disrupted [24–26]. Recently, there has been a renewed interest in using mannitol as a hyperosmotic agent to selectively open BBB near lesions in the central nervous system (CNS) through intra-arterial catheterization [75]. It was reported that a single injection of mannitol could result in an effective transient BBBO for 30 to 60 min, which returned to baseline completely in 2 to 10 h [76]. Catheter position, infusion speed, and infusion volume collectively determine the spatial distribution and extent of BBBO [16–18]. In an OBBBO treatment, if injected at an excessive amount, mannitol tends to leak into the region via the opened BBB. Our study concurred with this knowledge and showed as high as 70 mM mannitol could leaked to the brain parenchyma. Brain accumulation of mannitol was shown to be associated with consequent increase in water content or edema (indicated by increased regional T_1 and T_2 times). These findings are consistent with previously reported mannitol accumulation in the acute cerebral ischemia [30] or brain tumors and surrounding peritumoral edematous parenchyma [28,29]. In contrast,

when the infusion volume was relatively small (i.e., 1 mL of 25% mannitol or less), the leakage of mannitol into the interstitial space was found insignificant, correlating well with CEST MRI observation. Yet this dose was still sufficient to open the BBB as evidenced by gadolinium contrast. Therefore, CEST MRI provides a useful non-invasive imaging tool to optimize a mannitol-based BBBO treatment in which efficacy and adverse effects are properly balanced. Of note, the infusion time is also a critical factor, and extended infusion time can lead to thrombus formation and thereby ischemia. In fact, our MRS result (Figure 4b) revealed the augmented production and accumulation of lactate (1.3 ppm) in the ipsilateral hemisphere in some rats receiving a high dose (3 mL) using a long infusion time (5 min), indicative of ischemia.

CEST MRI provides an effective non-invasive imaging tool for specifically assessing the amount of mannitol accumulated in tissues, which is of clinical significance. The methods currently being used in the clinic, including serum osmolality or osmolar gap, are invasive and indirect. Only a few electrochemical-sensors-based [77] or enzyme-based (e.g., mannitol dehydrogenase) [24] *ex vivo* methods have been developed to date, but none of them enters clinical applications yet. Only few mannitol-detecting MRI methods have been reported previously. For instance, chemical shift imaging has been demonstrated to detect the spatial distribution of mannitol in acute cerebral ischemia [30] and meningioma [29]. However, low spatial and temporal resolution hinders the widespread clinical use of the ^1H -MRS/CSI method. Compared to ^1H MRS, CEST MRI has relatively higher sensitivity, higher spatial resolution, and shorter acquisition time; hence it is more suitable for monitoring mannitol distribution *in vivo* in a clinical setting. Spin-lock (CESL) MRI has also been used to detect D-mannitol [36,78]. CEST and CESL MRI are inherently very similar, with both methods detecting exchangeable protons. In the CESL studies by Jin [36,78], mannitol was used as an osmolality control to investigate the contribution of altered tissue water content to the apparent $\Delta R1\rho$. Being used as an intravascular agent in those studies, no quantitative detection of tissue mannitol was performed. Here, we applied CEST MRI for detecting mannitol accumulated in the brain. Our study is the first attempt to perform quantitative analyses of tissue-accumulated mannitol using label-free CEST MRI directly by its hydroxyl protons. Further technical optimization is warranted to improve the accuracy of quantification. For example, we observed relatively large variations using a 6-pool Bloch fitting, likely due to low SNR of pixel-wise CEST data. We then demonstrated that AREX (also called $\text{AREX}_{\text{asym}}$) was helpful in reducing the influence of T_1 and T_2 . Still, future studies are needed to convert the measured AREX values into mannitol concentrations and validate such quantitation. Another technical hurdle is the potentially low sensitivity of CEST MRI detection at low field strengths, such as 3T. For example, the simulation (Figure S5) showed that the sensitivity may be as much as three times lower at 3T than at 9.4T. While previous studies on glucose-enhanced CEST MRI were successful at 3T scanners, both preclinically [79] and clinically [49,80], it will require a higher concentration to generate sufficiently high CEST MRI at 3T. One possible solution is to use advanced CEST MRI methods, such as CESL and on-resonance variable delay multipulse (VDMP), which may be more suitable for detecting fast exchangeable protons, such as hydroxyl protons, at 3T [48,78].

Lastly, the present approach could be particularly useful when OBBBO is combined with the delivery of chemotherapy agents that can be detected by MRI based on their inherent CEST signatures, such as gemcitabine [81,82], pemetrexed [83], olsalazine [84], and melphalan [85], just to name a few. The combined CEST could concurrently optimize mannitol dosing, the timing and dosing of the anticancer agent to be delivered and assess whether therapeutically desirable drug levels are achieved within the target volume. Generating such data is not only crucial for individualized medicine, but was also recently recommended as one of the baseline requirements for novel agents to be considered for phase II/III brain cancer efficacy trials [2].

It should be noted that accurate determination of the concentration of mannitol using CEST MRI is not always straightforward because the CEST MRI signal is affected by a

wide variety of factors. For example, T_1 is known to strongly affect CEST quantification. In our study, we found the tissue T_1 and T_2 relaxation times were markedly increased in the high dose group, attributed to edema formation. In this context, T_1 -compensated methods such as the T_1 compensated inverse Z-analysis (AREX) can be used to reduce the potential influence of tissue T_1 changes [59–61]. Our results showed that in the regions with strong T_1 changes, the degree of Δ AREX increase was much smaller than that of Δ MTR_{asym}, indicative of an overestimation of mannitol accumulation when the non- T_1 -compensated MTR_{asym} was used. However, both methods show consistent spatial distribution of mannitol (Figure 8). The AREX-based analyses also showed significantly elevated CEST in the ipsilateral hemispheres compared to the contralateral hemisphere in the high mannitol dosing group, suggesting the observed CEST signal change was mainly the result of mannitol accumulation than tissue T_1 changes. Moreover, we utilized Bloch equation fitting to extract mannitol concentration in the tissue. This method takes all factors, such as T_1 , T_2 , tissue water content, and other exchangeable protons, into consideration and hence potentially provides more accurate quantification of mannitol concentration. Indeed, the computed mannitol concentrations were in good agreement with MRS measurement. Tissue pH might also affect the accuracy of quantification. While both intracellular and extracellular pH values in the healthy brain are constant [24], pathological changes such as acute ischemia can cause tissue pH to vary significantly [86]. Hence, caution has to be taken to quantify the mannitol concentration in different compartments. Injecting a relatively large volume of mannitol solution may also cause a transient change in the blood pH (normal range ~7.4) because the solution has a relatively acidic pH of 5.9 (4.5 to 7.0). However, the CEST MRI detection was performed 20 min later; hence, this transient pH change is unlikely to impact our CEST MRI measurement significantly. All those factors should be considered when converting the measured CEST signal to mannitol concentration. Given that the NMR signals of non-exchangeable protons acquired by ^1H -MRS are not prone to these factors, combining CEST and MRS can achieve both quantification accuracy and high spatial/temporal resolution for detecting mannitol.

5. Conclusions

We characterized the CEST MRI contrast of mannitol and demonstrated that CEST MRI could be used for non-invasive, label-free detection of mannitol accumulated in the brain parenchyma following OBBBO. Thus, the present CEST MRI method provides a tool for monitoring the brain uptake of mannitol and adjusting the dose in mannitol-based treatments to obtain optimized efficacy and safety. Furthermore, there is traction to move guidance of IA infusions to cerebral vasculature from the current X-ray routine toward real-time MRI guidance. In this new environment, the reported MRI method has potential for improving the safety profile of OBBBO by continuously monitoring mannitol accumulation in the brain. It could be combined with previously described, drug-detecting CEST techniques to confirm adequate drug delivery after OBBBO.

Supplementary Materials: The following supporting information can be downloaded at: <https://www.mdpi.com/article/10.3390/pharmaceutics14112529/s1>, References [87–92] are cited in the supplementary materials. Figure S1. Bloch fitting (lines) of the experiment data (solid dots) of 20 mM mannitol at pH 7.2 (37 °C, PBS). Figure S2. Optimization of CEST MRI detection of mannitol. Figure S3. R_1 and R_2 relaxation rates of mannitol at different concentrations at pH 7.2 (37 °C, PBS). Figure S4. Estimation of the change in hydroxyl proton concentration due to mannitol accumulation in the brain by Bloch fitting of Z-spectral data. Figure S5. Comparison of the CEST signal at 3T and 9.4T.

Author Contributions: Conceptualization, J.L., M.J. and G.L.; methodology, P.W., M.J., J.X., D.O.K. and G.L.; software, J.L., C.C., C.B., J.Z., L.C., formal analysis, J.L., C.C., J.Z., C.B., S.A., J.X., D.O.K., P.C.M.v.Z., P.W., M.J. and G.L.; data curation, J.L., S.A., C.B. and G.L.; writing—original draft preparation, J.L., M.J. and G.L.; writing—review and editing, S.A., D.O.K., P.C.M.v.Z., P.W., M.J. and G.L.; supervision, G.L.; project administration, P.C.M.v.Z., P.W., M.J. and G.L.; funding acquisition, G.L. and P.C.M.v.Z.; All authors have read and agreed to the published version of the manuscript.

Funding: This work was supported by NIH grants R21CA215860, R01EB019934, and EB015032. J Liu was supported by Natural Science Foundation of Guangdong Province 2019A151511161.

Institutional Review Board Statement: All animal study protocols used in this study were approved by the Johns Hopkins University's Institutional Animal Care and Use Committee. (protocol# RA15M183, date of approval: 12 June 2015).

Informed Consent Statement: Not applicable.

Data Availability Statement: Data presented in this study are available on request from the corresponding author.

Conflicts of Interest: The authors declare no conflict of interest.

References

1. Pardridge, W.M. Blood-brain barrier delivery. *Drug Discov. Today* **2007**, *12*, 54–61. [[CrossRef](#)] [[PubMed](#)]
2. Grossman, S.A.; Romo, C.G.; Rudek, M.A.; Supko, J.; Fisher, J.; Nabors, L.B.; Wen, P.Y.; Peereboom, D.M.; Ellingson, B.M.; Elmquist, W.; et al. Baseline requirements for novel agents being considered for phase II/III brain cancer efficacy trials: Conclusions from the Adult Brain Tumor Consortium's first workshop on CNS drug delivery. *Neuro Oncol.* **2020**, *22*, 1422–1424. [[CrossRef](#)] [[PubMed](#)]
3. Gu, J.; Huang, H.; Huang, Y.; Sun, H.; Xu, H. Hypertonic saline or mannitol for treating elevated intracranial pressure in traumatic brain injury: A meta-analysis of randomized controlled trials. *Neurosurg. Rev.* **2019**, *42*, 499–509. [[CrossRef](#)]
4. Videen, T.O.; Zazulia, A.R.; Manno, E.M.; Derdeyn, C.P.; Adams, R.E.; Diringer, M.N.; Powers, W.J. Mannitol bolus preferentially shrinks non-infarcted brain in patients with ischemic stroke. *Neurology* **2001**, *57*, 2120–2122. [[CrossRef](#)] [[PubMed](#)]
5. Esquenazi, Y.; Lo, V.P.; Lee, K. Critical Care Management of Cerebral Edema in Brain Tumors. *J. Intensive Care Med.* **2017**, *32*, 15–24. [[CrossRef](#)] [[PubMed](#)]
6. Witherspoon, B.; Ashby, N.E. The use of mannitol and hypertonic saline therapies in patients with elevated intracranial pressure: A review of the evidence. *Nurs. Clin.* **2017**, *52*, 249–260. [[CrossRef](#)]
7. Cook, A.M.; Morgan Jones, G.; Hawryluk, G.W.J.; Mailloux, P.; McLaughlin, D.; Papangelou, A.; Samuel, S.; Tokumaru, S.; Venkatasubramanian, C.; Zacko, C.; et al. Guidelines for the Acute Treatment of Cerebral Edema in Neurocritical Care Patients. *Neurocrit. Care* **2020**, *32*, 647–666. [[CrossRef](#)]
8. Rapoport, S.I.; Hori, M.; Klatzo, I. Testing of a hypothesis for osmotic opening of the blood-brain barrier. *Am. J. Physiol.* **1972**, *223*, 323–331. [[CrossRef](#)]
9. Burkhardt, J.-K.; Riina, H.; Shin, B.J.; Christos, P.; Kesavabhotla, K.; Hofstetter, C.P.; Tsiouris, A.J.; Boockvar, J.A. Intra-arterial delivery of bevacizumab after blood-brain barrier disruption for the treatment of recurrent glioblastoma: Progression-free survival and overall survival. *World Neurosurg.* **2012**, *77*, 130–134. [[CrossRef](#)]
10. Neuwelt, E.A.; Frenkel, E.P.; Diehl, J.T.; Maravilla, K.R.; Vu, L.H.; Clark, W.K.; Rapoport, S.I.; Barnett, P.A.; Hill, S.A.; Lewis, S.E.; et al. Osmotic blood-brain barrier disruption: A new means of increasing chemotherapeutic agent delivery. *Trans. Am. Neurol. Assoc.* **1979**, *104*, 256–260.
11. Doolittle, N.D.; Miner, M.E.; Hall, W.A.; Siegal, T.; Hanson, E.J.; Osztie, E.; McAllister, L.D.; Bubalo, J.S.; Kraemer, D.F.; Fortin, D.; et al. Safety and efficacy of a multicenter study using intraarterial chemotherapy in conjunction with osmotic opening of the blood-brain barrier for the treatment of patients with malignant brain tumors. *Cancer* **2000**, *88*, 637–647. [[CrossRef](#)]
12. Charest, G.; Sanche, L.; Fortin, D.; Mathieu, D.; Paquette, B. Optimization of the route of platinum drugs administration to optimize the concomitant treatment with radiotherapy for glioblastoma implanted in the Fischer rat brain. *J. Neurooncol.* **2013**, *115*, 365–373. [[CrossRef](#)] [[PubMed](#)]
13. Lesniak, W.G.; Chu, C.; Jablonska, A.; Du, Y.; Pomper, M.G.; Walczak, P.; Janowski, M. A Distinct Advantage to Intraarterial Delivery of (89)Zr-Bevacizumab in PET Imaging of Mice With and Without Osmotic Opening of the Blood-Brain Barrier. *J. Nucl. Med.* **2019**, *60*, 617–622. [[CrossRef](#)] [[PubMed](#)]
14. Lesniak, W.G.; Chu, C.; Jablonska, A.; Behnam Azad, B.; Zwaenepoel, O.; Zawadzki, M.; Lisok, A.; Pomper, M.G.; Walczak, P.; Gettemans, J.; et al. PET imaging of distinct brain uptake of a nanobody and similarly-sized PAMAM dendrimers after intra-arterial administration. *Eur. J. Nucl. Med. Mol. Imaging* **2019**, *46*, 1940–1951. [[CrossRef](#)] [[PubMed](#)]
15. Hersh, D.S.; Wadajkar, A.S.; Roberts, N.; Perez, J.G.; Connolly, N.P.; Frenkel, V.; Winkles, J.A.; Woodworth, G.F.; Kim, A.J. Evolving Drug Delivery Strategies to Overcome the Blood Brain Barrier. *Curr. Pharm. Des.* **2016**, *22*, 1177–1193. [[CrossRef](#)] [[PubMed](#)]
16. Chen, L.; Liu, J.; Chu, C.; Han, Z.; Yadav, N.; Xu, J.; Bai, R.; Staedtke, V.; Pearl, M.; Walczak, P.; et al. Deuterium oxide as a contrast medium for real-time MRI-guided endovascular neurointervention. *Theranostics* **2021**, *11*, 6240–6250. [[CrossRef](#)] [[PubMed](#)]
17. Chu, C.; Jablonska, A.; Lesniak, W.G.; Thomas, A.M.; Lan, X.; Linville, R.M.; Li, S.; Searson, P.C.; Liu, G.; Pearl, M.; et al. Optimization of osmotic blood-brain barrier opening to enable intravital microscopy studies on drug delivery in mouse cortex. *J. Control. Release* **2020**, *317*, 312–321. [[CrossRef](#)]
18. Chu, C.; Liu, G.; Janowski, M.; Bulte, J.W.M.; Li, S.; Pearl, M.; Walczak, P. Real-Time MRI Guidance for Reproducible Hyperosmolar Opening of the Blood-Brain Barrier in Mice. *Front. Neurol.* **2018**, *9*, 921. [[CrossRef](#)]

19. Janowski, M.; Walczak, P.; Pearl, M.S. Predicting and optimizing the territory of blood-brain barrier opening by superselective intra-arterial cerebral infusion under dynamic susceptibility contrast MRI guidance. *J. Cereb. Blood Flow Metab.* **2016**, *36*, 569–575. [[CrossRef](#)]
20. Zawadzki, M.; Walecki, J.; Kostkiewicz, B.; Kostyra, K.; Pearl, M.S.; Solaiyappan, M.; Walczak, P.; Janowski, M. Real-time MRI guidance for intra-arterial drug delivery in a patient with a brain tumor: Technical note. *BMJ Case Rep.* **2019**, *12*. [[CrossRef](#)]
21. Zawadzki, M.; Walecki, J.; Kostkiewicz, B.; Kostyra, K.; Walczak, P.; Janowski, M. Follow-up of intra-arterial delivery of bevacizumab for treatment of butterfly glioblastoma in patient with first-in-human, real-time MRI-guided intra-arterial neurointervention. *J. Neurointerv. Surg.* **2021**, *13*, 1037–1039. [[CrossRef](#)] [[PubMed](#)]
22. Node, Y.; Nakazawa, S. Clinical study of mannitol and glycerol on raised intracranial pressure and on their rebound phenomenon. *Adv. Neurol.* **1990**, *52*, 359–363. [[PubMed](#)]
23. Grande, P.O.; Romner, B. Osmotherapy in brain edema: A questionable therapy. *J. Neurosurg. Anesthesiol.* **2012**, *24*, 407–412. [[CrossRef](#)]
24. Cho, J.; Kim, Y.H.; Han, H.S.; Park, J. Accumulated mannitol and aggravated cerebral edema in a rat model of middle cerebral artery infarction. *J. Korean Neurosurg. Soc.* **2007**, *42*, 337–341. [[CrossRef](#)]
25. Kaufmann, A.M.; Cardoso, E.R. Aggravation of vasogenic cerebral edema by multiple-dose mannitol. *J. Neurosurg.* **1992**, *77*, 584–589. [[CrossRef](#)]
26. Palma, L.; Bruni, G.; Fiaschi, A.I.; Mariottini, A. Passage of mannitol into the brain around gliomas: A potential cause of rebound phenomenon. A study on 21 patients. *J. Neurosurg. Sci.* **2006**, *50*, 63–66. [[PubMed](#)]
27. Garcia-Morales, E.J.; Cariappa, R.; Parvin, C.A.; Scott, M.G.; Diringner, M.N. Osmole gap in neurologic-neurosurgical intensive care unit: Its normal value, calculation, and relationship with mannitol serum concentrations. *Crit. Care Med.* **2004**, *32*, 986–991. [[CrossRef](#)] [[PubMed](#)]
28. Peeling, J.; Sutherland, G. High-resolution ¹H NMR spectroscopy studies of extracts of human cerebral neoplasms. *Magn. Reson. Med.* **1992**, *24*, 123–136. [[CrossRef](#)]
29. Sankar, T.; Assina, R.; Karis, J.P.; Theodore, N.; Preul, M.C. Neurosurgical implications of mannitol accumulation within a meningioma and its peritumoral region demonstrated by magnetic resonance spectroscopy: Case report. *J. Neurosurg.* **2008**, *108*, 1010–1013. [[CrossRef](#)]
30. Maioriello, A.V.; Chaljub, G.; Nauta, H.J.; Lacroix, M. Chemical shift imaging of mannitol in acute cerebral ischemia. Case report. *J. Neurosurg.* **2002**, *97*, 687–691. [[CrossRef](#)]
31. Ward, K.M.; Aletras, A.H.; Balaban, R.S. A new class of contrast agents for MRI based on proton chemical exchange dependent saturation transfer (CEST). *J. Magn. Reson.* **2000**, *143*, 79–87. [[CrossRef](#)] [[PubMed](#)]
32. van Zijl, P.C.; Yadav, N.N. Chemical exchange saturation transfer (CEST): What is in a name and what isn't? *Magn. Reson. Med.* **2011**, *65*, 927–948. [[CrossRef](#)] [[PubMed](#)]
33. van Zijl, P.C.; Jones, C.K.; Ren, J.; Malloy, C.R.; Sherry, A.D. MRI detection of glycogen in vivo by using chemical exchange saturation transfer imaging (glycoCEST). *Proc. Natl. Acad. Sci. USA* **2007**, *104*, 4359–4364. [[CrossRef](#)]
34. Chan, K.W.; McMahon, M.T.; Kato, Y.; Liu, G.; Bulte, J.W.; Bhujwalla, Z.M.; Artemov, D.; van Zijl, P.C. Natural D-glucose as a biodegradable MRI contrast agent for detecting cancer. *Magn. Reson. Med.* **2012**, *68*, 1764–1773. [[CrossRef](#)] [[PubMed](#)]
35. Walker-Samuel, S.; Ramasawmy, R.; Torrealdea, F.; Rega, M.; Rajkumar, V.; Johnson, S.P.; Richardson, S.; Goncalves, M.; Parkes, H.G.; Arstad, E.; et al. In vivo imaging of glucose uptake and metabolism in tumors. *Nat. Med.* **2013**, *19*, 1067–1072. [[CrossRef](#)]
36. Jin, T.; Mehrens, H.; Wang, P.; Kim, S.G. Glucose metabolism-weighted imaging with chemical exchange-sensitive MRI of 2-deoxyglucose (2DG) in brain: Sensitivity and biological sources. *NeuroImage* **2016**, *143*, 82–90. [[CrossRef](#)] [[PubMed](#)]
37. Nasrallah, F.A.; Pages, G.; Kuchel, P.W.; Golay, X.; Chuang, K.H. Imaging brain deoxyglucose uptake and metabolism by glucoCEST MRI. *J. Cereb. Blood Flow Metab.* **2013**, *33*, 1270–1278. [[CrossRef](#)]
38. Rivlin, M.; Horev, J.; Tsarfaty, I.; Navon, G. Molecular imaging of tumors and metastases using chemical exchange saturation transfer (CEST) MRI. *Sci. Rep.* **2013**, *3*, 3045. [[CrossRef](#)]
39. Rivlin, M.; Navon, G. CEST MRI of 3-O-methyl-D-glucose on different breast cancer models. *Magn. Reson. Med.* **2018**, *79*, 1061–1069. [[CrossRef](#)]
40. Rivlin, M.; Tsarfaty, I.; Navon, G. Functional molecular imaging of tumors by chemical exchange saturation transfer MRI of 3-O-Methyl-D-glucose. *Magn. Reson. Med.* **2014**, *72*, 1375–1380. [[CrossRef](#)]
41. Rivlin, M.; Navon, G. Glucosamine and N-acetyl glucosamine as new CEST MRI agents for molecular imaging of tumors. *Sci. Rep.* **2016**, *6*, 32648. [[CrossRef](#)] [[PubMed](#)]
42. Han, Z.; Zhang, S.; Fujiwara, K.; Zhang, J.; Li, Y.; Liu, J.; van Zijl, P.C.M.; Lu, Z.R.; Zheng, L.; Liu, G. Extradomain-B Fibronectin-Targeted Dextran-Based Chemical Exchange Saturation Transfer Magnetic Resonance Imaging Probe for Detecting Pancreatic Cancer. *Bioconjug. Chem.* **2019**, *30*, 1425–1433. [[CrossRef](#)] [[PubMed](#)]
43. Chen, H.; Liu, D.; Li, Y.; Xu, X.; Xu, J.; Yadav, N.N.; Zhou, S.; van Zijl, P.C.M.; Liu, G. CEST MRI monitoring of tumor response to vascular disrupting therapy using high molecular weight dextrans. *Magn. Reson. Med.* **2019**, *82*, 1471–1479. [[CrossRef](#)]
44. Li, Y.; Qiao, Y.; Chen, H.; Bai, R.; Staedtke, V.; Han, Z.; Xu, J.; Chan, K.W.Y.; Yadav, N.; Bulte, J.W.M.; et al. Characterization of tumor vascular permeability using natural dextrans and CEST MRI. *Magn. Reson. Med.* **2018**, *79*, 1001–1009. [[CrossRef](#)] [[PubMed](#)]

45. Liu, G.; Banerjee, S.R.; Yang, X.; Yadav, N.; Lisok, A.; Jablonska, A.; Xu, J.; Li, Y.; Pomper, M.G.; van Zijl, P. A dextran-based probe for the targeted magnetic resonance imaging of tumours expressing prostate-specific membrane antigen. *Nat. Biomed Eng.* **2017**, *1*, 977–982. [[CrossRef](#)] [[PubMed](#)]
46. Han, Z.; Liu, G. Sugar-based biopolymers as novel imaging agents for molecular magnetic resonance imaging. *Wiley. Interdiscip. Rev. Nanomed. Nanobiotechnol.* **2019**, *11*, e1551. [[CrossRef](#)] [[PubMed](#)]
47. Liu, G.; Bettegowda, C.; Qiao, Y.; Staedtke, V.; Chan, K.W.; Bai, R.; Li, Y.; Riggins, G.J.; Kinzler, K.W.; Bulte, J.W.; et al. Noninvasive imaging of infection after treatment with tumor-homing bacteria using Chemical Exchange Saturation Transfer (CEST) MRI. *Magn. Reson. Med.* **2013**, *70*, 1690–1698. [[CrossRef](#)]
48. Herz, K.; Lindig, T.; Deshmane, A.; Schittenhelm, J.; Skardelly, M.; Bender, B.; Ernemann, U.; Scheffler, K.; Zaiss, M. T1rho-based dynamic glucose-enhanced (DGERho) MRI at 3 T: Method development and early clinical experience in the human brain. *Magn. Reson. Med.* **2019**, *82*, 1832–1847. [[CrossRef](#)]
49. Xu, X.; Sehgal, A.A.; Yadav, N.N.; Larterra, J.; Blair, L.; Blakeley, J.; Seidemo, A.; Coughlin, J.M.; Pomper, M.G.; Knutsson, L.; et al. d-glucose weighted chemical exchange saturation transfer (glucoCEST)-based dynamic glucose enhanced (DGE) MRI at 3T: Early experience in healthy volunteers and brain tumor patients. *Magn. Reson. Med.* **2020**, *84*, 247–262. [[CrossRef](#)]
50. Walczak, P.; Wojtkiewicz, J.; Nowakowski, A.; Habich, A.; Holak, P.; Xu, J.; Adamiak, Z.; Chehade, M.; Pearl, M.S.; Gailloud, P.; et al. Real-time MRI for precise and predictable intra-arterial stem cell delivery to the central nervous system. *J. Cereb. Blood Flow Metab.* **2017**, *37*, 2346–2358. [[CrossRef](#)]
51. Liu, G.; Gilad, A.A.; Bulte, J.W.; van Zijl, P.C.; McMahon, M.T. High-throughput screening of chemical exchange saturation transfer MR contrast agents. *Contrast Media Mol. Imaging* **2010**, *5*, 162–170. [[CrossRef](#)] [[PubMed](#)]
52. Kim, M.; Gillen, J.; Landman, B.A.; Zhou, J.; van Zijl, P.C. Water saturation shift referencing (WASSR) for chemical exchange saturation transfer (CEST) experiments. *Magn. Reson. Med.* **2009**, *61*, 1441–1450. [[CrossRef](#)] [[PubMed](#)]
53. Zhang, J.; Li, Y.; Slania, S.; Yadav, N.N.; Liu, J.; Wang, R.; Zhang, J.; Pomper, M.G.; van Zijl, P.C.; Yang, X.; et al. Phenols as Diamagnetic T2 -Exchange Magnetic Resonance Imaging Contrast Agents. *Chemistry (Easton)* **2018**, *24*, 1259–1263.
54. Cloyd, J.C.; Snyder, B.D.; Cleeremans, B.; Bundlie, S.R.; Blomquist, C.H.; Lakatua, D.J. Mannitol pharmacokinetics and serum osmolality in dogs and humans. *J. Pharmacol. Exp. Ther.* **1986**, *236*, 301–306. [[PubMed](#)]
55. Better, O.S.; Rubinstein, I.; Winaver, J.M.; Knochel, J.P. Mannitol therapy revisited (1940–1997). *Kidney Int.* **1997**, *52*, 886–894. [[CrossRef](#)]
56. Obach, R.S.; Baxter, J.G.; Liston, T.E.; Silber, B.M.; Jones, B.C.; MacIntyre, F.; Rance, D.J.; Wastall, P. The prediction of human pharmacokinetic parameters from preclinical and in vitro metabolism data. *J. Pharmacol. Exp. Ther.* **1997**, *283*, 46–58.
57. Chen, L.; Zeng, H.; Xu, X.; Yadav, N.N.; Cai, S.; Puts, N.A.; Barker, P.B.; Li, T.; Weiss, R.G.; van Zijl, P.C.M.; et al. Investigation of the contribution of total creatine to the CEST Z-spectrum of brain using a knockout mouse model. *NMR Biomed.* **2017**, *30*, e3834. [[CrossRef](#)]
58. Miller, C.O.; Cao, J.; Chekmenev, E.Y.; Damon, B.M.; Cherrington, A.D.; Gore, J.C. Noninvasive measurements of glycogen in perfused mouse livers using chemical exchange saturation transfer NMR and comparison to (13)C NMR spectroscopy. *Anal. Chem.* **2015**, *87*, 5824–5830. [[CrossRef](#)]
59. Zaiss, M.; Xu, J.; Goerke, S.; Khan, I.S.; Singer, R.J.; Gore, J.C.; Gochberg, D.F.; Bachert, P. Inverse Z-spectrum analysis for spillover-, MT-, and T1 -corrected steady-state pulsed CEST-MRI-application to pH-weighted MRI of acute stroke. *NMR Biomed.* **2014**, *27*, 240–252. [[CrossRef](#)]
60. Lee, D.H.; Heo, H.Y.; Zhang, K.; Zhang, Y.; Jiang, S.; Zhao, X.; Zhou, J. Quantitative assessment of the effects of water proton concentration and water T1 changes on amide proton transfer (APT) and nuclear overhauser enhancement (NOE) MRI: The origin of the APT imaging signal in brain tumor. *Magn. Reson. Med.* **2017**, *77*, 855–863. [[CrossRef](#)]
61. Wu, R.; Liu, C.M.; Liu, P.K.; Sun, P.Z. Improved measurement of labile proton concentration-weighted chemical exchange rate (k(ws)) with experimental factor-compensated and T(1) -normalized quantitative chemical exchange saturation transfer (CEST) MRI. *Contrast Media Mol. Imaging* **2012**, *7*, 384–389. [[CrossRef](#)] [[PubMed](#)]
62. Zaiss, M. CEST Sources. 2014. Available online: <http://www.cest-sources.org> (accessed on 1 February 2022).
63. Bie, C.; Li, Y.; Zhou, Y.; Bhujwala, Z.M.; Song, X.; Liu, G.; van Zijl, P.C.M.; Yadav, N.N. Deep learning-based classification of preclinical breast cancer tumor models using chemical exchange saturation transfer magnetic resonance imaging. *NMR Biomed.* **2022**, *35*, e4626. [[CrossRef](#)] [[PubMed](#)]
64. Shah, S.M.; Mougou, O.E.; Carradus, A.J.; Geades, N.; Dury, R.; Morley, W.; Gowland, P.A. The z-spectrum from human blood at 7T. *NeuroImage* **2018**, *167*, 31–40. [[CrossRef](#)]
65. van Zijl, P.C.M.; Lam, W.W.; Xu, J.; Knutsson, L.; Stanisiz, G.J. Magnetization Transfer Contrast and Chemical Exchange Saturation Transfer MRI. Features and analysis of the field-dependent saturation spectrum. *NeuroImage* **2018**, *168*, 222–241. [[CrossRef](#)] [[PubMed](#)]
66. Xu, X.; Xu, J.; Chan, K.W.Y.; Liu, J.; Liu, H.; Li, Y.; Chen, L.; Liu, G.; van Zijl, P.C.M. GlucoCEST imaging with on-resonance variable delay multiple pulse (onVDMP) MRI. *Magn. Reson. Med.* **2019**, *81*, 47–56. [[CrossRef](#)]
67. Wishart, D.S.; Feunang, Y.D.; Marcu, A.; Guo, A.C.; Liang, K.; Vazquez-Fresno, R.; Sajed, T.; Johnson, D.; Li, C.; Karu, N.; et al. HMDB 4.0: The human metabolome database for 2018. *Nucleic Acids Res.* **2018**, *46*, D608–D617. [[CrossRef](#)] [[PubMed](#)]
68. Yadav, N.N.; Xu, J.; Bar-Shir, A.; Qin, Q.; Chan, K.W.; Grgac, K.; Li, W.; McMahon, M.T.; van Zijl, P.C. Natural D-glucose as a biodegradable MRI relaxation agent. *Magn. Reson. Med.* **2014**, *72*, 823–828. [[CrossRef](#)]

69. Xin, L.; Tkac, I. A practical guide to in vivo proton magnetic resonance spectroscopy at high magnetic fields. *Anal. Biochem.* **2017**, *529*, 30–39. [[CrossRef](#)]
70. Hall, C.; Lueshen, E.; Mosat, A.; Linninger, A.A. Interspecies scaling in pharmacokinetics: A novel whole-body physiologically based modeling framework to discover drug biodistribution mechanisms in vivo. *J. Pharm. Sci.* **2012**, *101*, 1221–1241. [[CrossRef](#)]
71. Torre-Healy, A.; Marko, N.F.; Weil, R.J. Hyperosmolar therapy for intracranial hypertension. *Neurocrit. Care* **2012**, *17*, 117–130. [[CrossRef](#)]
72. Goldwasser, P.; Fotino, S. Acute renal failure following massive mannitol infusion. Appropriate response of tubuloglomerular feedback? *Arch. Intern. Med.* **1984**, *144*, 2214–2216. [[CrossRef](#)] [[PubMed](#)]
73. Whelan, T.V.; Bacon, M.E.; Madden, M.; Patel, T.G.; Handy, R. Acute renal failure associated with mannitol intoxication. Report of a case. *Arch. Intern. Med.* **1984**, *144*, 2053–2055. [[CrossRef](#)] [[PubMed](#)]
74. Perez-Perez, A.J.; Pazos, B.; Sobrado, J.; Gonzalez, L.; Gandara, A. Acute renal failure following massive mannitol infusion. *Am. J. Nephrol.* **2002**, *22*, 573–575. [[CrossRef](#)]
75. Joshi, S.; Meyers, P.M.; Ornstein, E. Intracarotid delivery of drugs: The potential and the pitfalls. *Anesthesiology* **2008**, *109*, 543–564. [[CrossRef](#)]
76. Siegal, T.; Rubinstein, R.; Bokstein, F.; Schwartz, A.; Lossos, A.; Shalom, E.; Chisin, R.; Gomori, J.M. In vivo assessment of the window of barrier opening after osmotic blood-brain barrier disruption in humans. *J. Neurosurg.* **2000**, *92*, 599–605. [[CrossRef](#)] [[PubMed](#)]
77. Beluomini, M.A.; da Silva, J.L.; Sedenho, G.C.; Stradiotto, N.R. D-mannitol sensor based on molecularly imprinted polymer on electrode modified with reduced graphene oxide decorated with gold nanoparticles. *Talanta* **2017**, *165*, 231–239. [[CrossRef](#)]
78. Jin, T.; Mehrens, H.; Hendrich, K.S.; Kim, S.G. Mapping brain glucose uptake with chemical exchange-sensitive spin-lock magnetic resonance imaging. *J. Cereb. Blood Flow Metab.* **2014**, *34*, 1402–1410. [[CrossRef](#)]
79. Huang, J.; van Zijl, P.C.M.; Han, X.; Dong, C.M.; Cheng, G.W.Y.; Tse, K.H.; Knutsson, L.; Chen, L.; Lai, J.H.C.; Wu, E.X.; et al. Altered d-glucose in brain parenchyma and cerebrospinal fluid of early Alzheimer's disease detected by dynamic glucose-enhanced MRI. *Sci Adv.* **2020**, *6*, eaba3884. [[CrossRef](#)]
80. Bender, B.; Herz, K.; Deshmane, A.; Richter, V.; Tabatabai, G.; Schittenhelm, J.; Skardelly, M.; Scheffler, K.; Ernemann, U.; Kim, M.; et al. GLINT: GlucoCEST in neoplastic tumors at 3 T—Clinical results of GlucoCEST in gliomas. *Magn. Reson. Mater. Phys. Biol. Med.* **2021**, *35*, 11–85. [[CrossRef](#)]
81. Li, Y.; Chen, H.; Xu, J.; Yadav, N.N.; Chan, K.W.; Luo, L.; McMahan, M.T.; Vogelstein, B.; van Zijl, P.C.; Zhou, S.; et al. CEST theranostics: Label-free MR imaging of anticancer drugs. *Oncotarget* **2016**, *7*, 6369–6378. [[CrossRef](#)]
82. Chen, Z.; Han, Z.; Liu, G. Repurposing Clinical Agents for Chemical Exchange Saturation Transfer Magnetic Resonance Imaging: Current Status and Future Perspectives. *Pharmaceutics* **2020**, *14*, 11. [[CrossRef](#)]
83. Lock, L.L.; Li, Y.; Mao, X.; Chen, H.; Staedtke, V.; Bai, R.; Ma, W.; Lin, R.; Li, Y.; Liu, G.; et al. One-Component Supramolecular Filament Hydrogels as Theranostic Label-Free Magnetic Resonance Imaging Agents. *ACS Nano* **2017**, *11*, 797–805. [[CrossRef](#)] [[PubMed](#)]
84. Yuan, Y.; Zhang, J.; Qi, X.; Li, S.; Liu, G.; Siddhanta, S.; Barman, I.; Song, X.; McMahan, M.T.; Bulte, J.W.M. Furin-mediated intracellular self-assembly of olsalazine nanoparticles for enhanced magnetic resonance imaging and tumour therapy. *Nat. Mater.* **2019**, *18*, 1376–1383. [[CrossRef](#)] [[PubMed](#)]
85. Ngen, E.J.; Bar-Shir, A.; Jablonska, A.; Liu, G.; Song, X.; Ansari, R.; Bulte, J.W.M.; Janowski, M.; Pearl, M.; Walczak, P.; et al. Imaging the DNA Alkylator Melphalan by CEST MRI: An Advanced Approach to Theranostics. *Mol. Pharm.* **2016**, *13*, 3043–3053. [[CrossRef](#)] [[PubMed](#)]
86. Kim, H.; Krishnamurthy, L.C.; Sun, P.Z. Brain pH Imaging and its Applications. *Neuroscience* **2021**, *474*, 51–62. [[CrossRef](#)]
87. Randtke, E.A.; Chen, L.Q.; Pagel, M.D. The reciprocal linear QUEST analysis method facilitates the measurements of chemical exchange rates with CEST MRI. *Contrast Media Mol Imaging* **2014**, *9*, 252–258. [[CrossRef](#)]
88. Zaiss, M.; Anemone, A.; Goerke, S.; Longo, D.L.; Herz, K.; Pohmann, R.; Aime, S.; Rivlin, M.; Navon, G.; Golay, X.; et al. Quantification of hydroxyl exchange of D-Glucose at physiological conditions for optimization of glucoCEST MRI at 3, 7 and 9.4 Tesla. *NMR Biomed.* **2019**, *32*, e4113. [[CrossRef](#)]
89. Zaiss, M.; Angelovski, G.; Demetriou, E.; McMahan, M.T.; Golay, X.; Scheffler, K. QUESP and QUEST revisited—Fast and accurate quantitative CEST experiments. *Magn. Reson. Med.* **2018**, *79*, 1708–1721. [[CrossRef](#)]
90. de Graaf, R.A.; Brown, P.B.; McIntyre, S.; Nixon, T.W.; Behar, K.L.; Rothman, D.L. High magnetic field water and metabolite proton T1 and T2 relaxation in rat brain in vivo. *Magn. Reson. Med.* **2006**, *56*, 386–394. [[CrossRef](#)]
91. Stanisz, G.J.; Odobina, E.E.; Pun, J.; Escaravage, M.; Graham, S.J.; Bronskill, M.J.; Henkelman, R.M. T1, T2 relaxation and magnetization transfer in tissue at 3T. *Magn. Reson. Med.* **2005**, *54*, 507–512. [[CrossRef](#)]
92. Hills, B.; Cano, C.; Belton, P. Proton NMR relaxation studies of aqueous polysaccharide systems. *Macromolecules* **1991**, *24*, 2944–2950. [[CrossRef](#)]